Efficient Solutions for Nonlocal Diffusion Problems Via Boundary-Adapted Spectral Methods

Siavash Jafarzadeh[1] · Adam Larios[2] · Florin Bobaru[1]

Abstract

We introduce an efficient boundary-adapted spectral method for peridynamic transient diffusion problems with arbitrary boundary conditions. The spectral approach transforms the convolution integral in the peridynamic formulation into a multiplication in the Fourier space, resulting in computations that scale as $O(N \log N)$. The limitation of regular spectral methods to periodic problems is eliminated using the volume penalization method. We show that arbitrary boundary conditions or volume constraints can be enforced in this way to achieve high levels of accuracy. To test the performance of our approach we compare the computational results with analytical solutions of the nonlocal problem. The performance is tested with convergence studies in terms of nodal discretization and the size of the penalization parameter in problems with Dirichlet and Neumann boundary conditions.

Keywords Peridynamics · Nonlocal diffusion · Spectral methods · Volume penalization

1 Introduction

Nonlocal models have been introduced to address certain phenomena which local models fail to describe satisfactorily. Delayed reaction-diffusion in biology [1], swarm of organisms [2], pedestrian traffic [3], flocking of birds [4–6], plane waves in solids [7], elasticity of nano-beams [8], and material damage [9, 10] are some examples of problems where nonlocal

---

✉ Adam Larios
  alarios@unl.edu

✉ Florin Bobaru
  fbobaru2@unl.edu

[1] Department of Mechanical and Materials Engineering, University of Nebraska-Lincoln, Lincoln, NE 68588-0526, USA

[2] Department of Mathematics, University of Nebraska-Lincoln, Lincoln, NE 68588-0130, USA

models are useful. Material damage models in particular are of significant interest, being used for failure prediction of critical materials and structures. Physical features in damage (evolving cracks and distributed failure) and small-scale heterogeneities can be naturally modeled using nonlocal approaches [11, 12], and would be otherwise difficult to describe or prohibitively expensive to compute with classical local approaches. Peridynamics, as a nonlocal extension of continuum mechanics [13, 14], has been successful in modeling damage evolution and material failure [13, 15, 16]. Dynamic brittle fracture [17–19], fatigue and thermally induced cracking [16, 20], fracture in porous and granular materials [21–23], failure of composites [24, 25], and corrosion damage [26–30] are among some applications of this formulation in modeling material damage.

In peridynamics (PD), material behavior at each point x depends on the interactions of that point with all of the points $\hat{x}$ in its neighborhood [14]. This neighborhood (usually a line segment in 1D, a disk in 2D, and a sphere in 3D) centered at x is called the "horizon region" of x and is denoted by H_x. H_x is the subdomain where nonlocal interactions exist for x.

Mathematical models of physical behavior using this approach are in the form of integro-differential equations, as spatial derivatives in the classical PDEs are replaced by convolution integrals that integrate the pairwise interactions of x with the points in H_x. Integration has significantly more relaxed smoothness and continuity requirements compared with differentiation, and hence, it allows for more robust handling of discontinuities, such as cracks. While nonlocality facilitates describing material degradation and provides certain advantages for incorporating small-scale features into large-scale models [31, 32], it also adds a significant computational cost, due to the convolution integral involved, compared with local models.

Two types of numerical methods have been commonly used for the discretization of PD models. One popular method that offers much flexibility for arbitrary/unguided damage/fracture evolution is a meshfree method based on the one-point Gaussian quadrature of the integral operator [33, 34]. If the total number of nodes in the domain is N and the number of nodes inside the horizon of each point is M, the computational cost at each time step in an explicit algorithm will be $O(NM)$. Note that in one-dimension, $= \frac{\delta}{L}N$, where L is the length of the domain and δ is the horizon size (see Fig. 1). Therefore, for a fixed horizon size, M itself varies as $O(N)$, and the computational cost is $O(N^2)$.

Finite element methods (FEM) have also been used to discretize PD models: in some of such models, each pairwise interaction (bond) is represented as a truss element [35, 36], while others use continuous or discontinuous Galerkin (DG) discretization methods, for example [37–39]. In all FEM-based discretizations of PD models, explicit solutions also cost $O(N^2)$ per time step. We note that regular FEM discretizations are not used for modeling of problems in which discontinuities appear due to the inherent difficulties of the method (see [37]). This is the main reason that only truss-based or DG methods have been used in PD models of failure/fracture, in addition to the most successful, meshfree discretization.

Coupling local models (discretized, e.g., with FEM) with PD models (discretized, e.g., with the meshfree method) has been seen as one way to increase the efficiency of simulations with PD models [40, 41]. These approaches are only beneficial when the region where nonlocality is helpful or dominates, covers only a small portion of the system modeled (e.g., small localized damage or crack growth). The advantage is lost in problems in which, for example, failure is affecting a large part of the domain [15, 19].

Note that in the methods mentioned above for discretizing nonlocal models, M increases exponentially with the problem's number of spatial dimensions. Indeed, assume that the length

Fig. 1 Nonlocal interactions of point x with its neighboring points $\hat{x}$ (in its horizon region H_x) in a schematic of a peridynamic body Ω
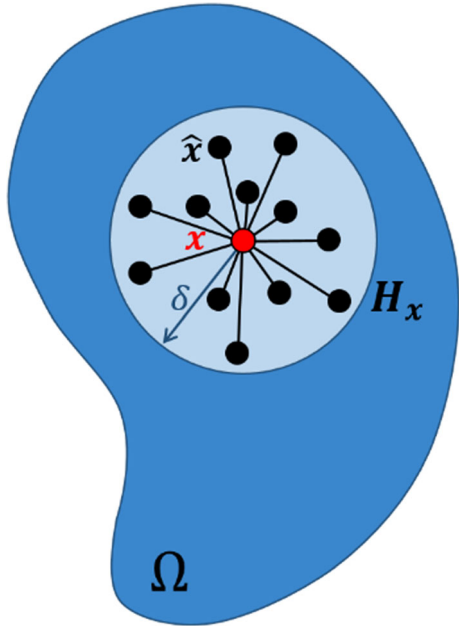
scale of the domain is L and the grid spacing in each direction is Δx. If δ is the radius of the neighborhood (also called the "horizon size", or simply "the horizon"), then $N = \left(\frac{L}{\Delta x}\right)^d$ and $M \propto \left(\frac{\delta}{\Delta x}\right)^d$ where d is the dimension of the problem. Computational cost per times step can then be expressed as $\left[\left(\frac{L}{\Delta x}\right)^d \cdot \left(\frac{\delta}{\Delta x}\right)^d\right]$.

In Fourier spectral methods, the solution is transformed to Fourier space (if the solution is assumed *periodic*), and the governing equations is reformulated based on the transformed solution. In the case of classical PDEs, spatial derivatives transform to multiplication operators, and the PDE reduces to a system of ODEs in Fourier space, which is far easier to solve [42]. For nonlocal models, Fourier transformation disentangles the convolution integral and reduces it to a multiplication in the spectral space. The only major cost in the spectral method is the Fourier transform itself, and its inverse. For this, the well-known *fast Fourier transform* (FFT) algorithms are available, at a cost of $O(N \log N)$ [42–44]. Not only is the cost of the Fourier spectral method significantly lower than the two other numerical methods used to discretize PD models, but the FFT is also easily parallelized, further increasing the potential advantages of this approach.

Although the spectral method seems to be a promising candidate for computing solutions to nonlocal problems, the assumption of periodicity limits its application. Most real-world problems are not periodic. A few recent studies have introduced Fourier spectral methods for periodic nonlocal models. For example, this method has been used for the nonlocal Allen-Cahn equation [45], nonlocal damage models [46], and peridynamic nonlocal operators for diffusion and wave propagation problems [47–50]. In all these cases, the problems considered were periodic. Spectral methods have also been used for the fractional-in-space reaction-diffusion equation in rectangular domains, where sine/cosine transforms were employed to impose homogeneous Dirichlet/

Neumann boundary conditions [51]. Another method, while not spectral, uses the FFT to diagonalize the stiffness matrixes arising in FE and collocation discretization methods for nonlocal problems with non-periodic boundary conditions [52, 53]. Although the order of computation is $N \log N$, the method is restricted to simple domain shapes like a square in 2D. The method is also dependent to the horizon shape. The authors of [52] state that the method is not applicable to domains with complex geometry, or to heterogeneous domains, and is challenging to use in 3D.

While the periodicity of the solution is inherent in Fourier spectral methods, there exist ways to overcome this limitation and apply them to general problems with complex domains and arbitrary boundary conditions [54–56]. *Volume penalization* is one such method.

Penalization methods have been used with the local Navier-Stokes PDE to introduce solid obstacles/boundaries in fluid flows, without changing the equations and discretization. A rigorous, simple volume-penalization method based on Brinkman model for flow in porous media [57] is developed by Angot et al. [58]. In [58], a large viscous term is added to the equation in the solid region to impose a Dirichlet (no-slip) boundary condition for the fluid-solid contact. Kevlahan and Ghidaglia [54] used this method with the Fourier spectral method in fluid dynamics problems. In these methods, the solution (velocity) is penalized by a substantially higher viscosity in the solid region to enforce a zero-velocity boundary condition. The method was applied for modeling flow over stationary or moving solid obstacles with complex geometries, inside periodic or confined fluid domains [59–61]. Volume penalization has also been used to enforce no-flux (Neumann-type) boundary conditions in advection-diffusion problems solved with the spectral method [62]. Another example for this efficient method is the 3D simulation of bumblebee flight in wind flow [63, 64].

In the present study, we introduce a spectral method to obtain efficient solutions to nonlocal equations of the peridynamic type for transient diffusion with arbitrary, non-periodic boundary conditions, using the volume-penalization technique. In Section 2, the PD formulation and boundary conditions implementation in PD problems are briefly discussed. Spectral methods and volume penalization for PD problems are introduced in Section 3. Stability analysis is provided in Section 4 and two examples with non-periodic BCs are solved in Section 5. Convergence studies are provided in Section 6.

2 Peridynamic Nonlocal Formulation

We start our development of spectral methods for peridynamic models with the PD diffusion equation in 1D. The methods described here are, however, applicable to other PD models, as well as to any other model with convolution integrals. Equation (1) is the general form of the PD diffusion equation in 1D [65]:

$$\frac{\partial u(x,t)}{\partial t} = \nu \mathcal{L}_\delta u(x,t) + f(x,t) \tag{1}$$

where x is the position in the 1D domain Ω, $u(x, t)$ is the unknown (the solution field) at point x and time t, ν is the diffusivity, $\mathcal{L}_\delta$ is the PD Laplacian operator (see below), and f is a source term. For a fixed time t, the PD Laplacian can be expressed as:

$$\mathcal{L}_\delta u(x) = \int_{H_x} \mu(\hat{x}-x)[u(\hat{x})-u(x)]\mathrm{d}\hat{x} \tag{2}$$

where $\mu(x)$ is a non-negative even function, called *the kernel function* that defines the nonlocal interactions in neighborhood of spatial points [65–67]. In this work, we take μ to be an integrable function with compact support. Since $\mu(\hat{x}-x) = \mu(x-\hat{x})$, we have:

$$\mathcal{L}_\delta u(x) = \int_{H_x} \mu(x-\hat{x}) u(\hat{x}) \mathrm{d}\hat{x} - u(x) \int_{H_x} \mu(x-\hat{x}) \mathrm{d}\hat{x} \tag{3}$$

Assume $\mu(x)$ is defined over $(-\infty, +\infty)$, with $\mu = 0$ outside of the horizon of $x=0$. With $\mu(x)$ being a given function, let $\beta = \int_{-\infty}^{+\infty} \mu(x)\mathrm{d}x$. The PD Laplacian becomes [66]:

$$\mathcal{L}_\delta u = \mu * u - \beta u \tag{4}$$

where $(*)$ denotes the convolution integral operation.

2.1 Peridynamic Boundary Conditions

In problems specified by classical local theories, constraints are in the form of boundary conditions imposed on the surfaces of the 3D domain. In nonlocal problems, constraints are in the form of specified values on regions outside of the domain, where they have nonlocal interactions with parts of the domain [68]. Therefore, in the nonlocal problems *constrained-volume* and *volume-constraints* are used instead of boundaries and boundary conditions, respectively [68]. Such description of course depends on the domain definition. For example, volume constraints may also be considered to be inside the domain. In this study however, the domain refers to the space where $u(x, t)$ is not specified and is solved for. Nevertheless, in many practical applications of peridynamics, imposing local-type boundary conditions is desired, for practical reasons.

Local boundary conditions can be enforced on a peridynamic body (Ω), for example, via extending the domain by δ in the normal direction of the surface $\partial\Omega$. Quantities on the constrained volume, which is the domain extension Γ, are specified such that the local boundary condition is effectively reproduced on $\partial\Omega$ [69–72]. Values on Γ are, in fact, volume constraints acting to enforce local boundary conditions. Figure 2 schematically shows the peridynamic body Ω, its boundary $\partial\Omega$, and the constrained-volume Γ.

Fig. 2 Schematic of a peridynamic domain (Ω), its boundary $(\partial\Omega)$, and its constrained volume (Γ)
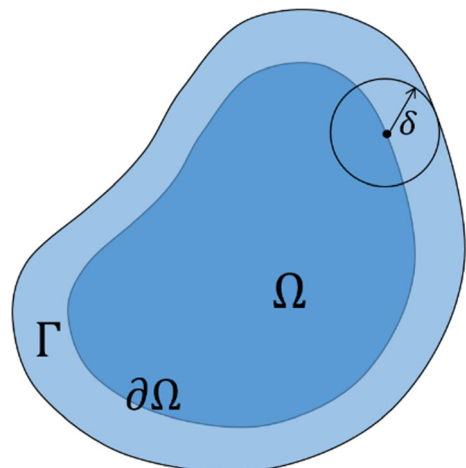
One way to impose volume constraints on Γ with minimal or no difference from imposing local boundary conditions on $\partial\Omega$, is the scheme discussed in [69, 70], known as the "fictitious nodes method." The terminology of this scheme refers to Γ as a "fictitious" region since it is not a part of the domain. Note that in 2D and 3D this method will not be exact except for the simplest geometries [70]. In this scheme, the volume constraints are implicit and time-dependent, i.e., values on Γ vary in time and are related to the values in the body Ω at that time. This type of implicit volume constraint can effectively impose a local BC on Ω. The enforcement of some local BCs using the fictitious region method for the one-dimensional case follows.

To enforce the local Dirichlet BC:

$$u(\cdot,t)|_{\partial\Omega} = u(\delta,t) = u_b \tag{5}$$

with respect to the 1D configuration in Fig. 3, and a given u_b, values on Γ should satisfy:

$$u(\cdot,t)|_{\Gamma} = u_{\Gamma}(x,t) = 2u_b - u(2\delta - x, t) \tag{6}$$

In order to apply the local Neumann BC:

$$\frac{\partial u}{\partial x}(\cdot,t)\Big|_{\partial\Omega} = \frac{\partial u}{\partial x}(\delta,t) = q_b, \tag{7}$$

given q_b, values in the constrained region are set as:

$$u(\cdot,t)|_{\Gamma} = u_{\Gamma}(x,t) = -2q_b(\delta - x) + u(2\delta - x, t) \tag{8}$$

With this approach, similar to the Dirichlet BC, the Neumann BC is imposed by assigning value of u rather than the values of its derivative. Note that Eq. (8) is new and different from the approach given in [69] where a source term is added in order to reproduce the Neumann BC. This specific form of Eq. (8) will show advantages when the spectral method will be used (see Section 3.2 below).

3 Spectral Method for Peridynamics with Volume Penalization

3.1 Spectral Method

Let $u(x,t)$ be a complex-valued function defined over the periodic domain $x \in T=[0,2\pi]$ with 0 identified with 2π, and evolve in time $t>0$. Then $u(x,t)$ can be expressed with the infinite Fourier series in space:

Fig. 3 Schematic for the fictitious domain (constrained volume Γ) and the peridynamic body Ω in 1D. Time-dependent values on Γ can be set to enforce some prescribed local boundary condition at $x=\delta$
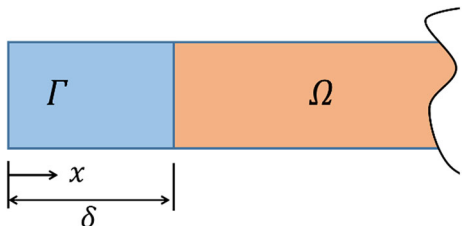
$$u(x,t) = \sum_{k=-\infty}^{+\infty} \breve{u}_k(t)\, e^{\zeta k x}, \qquad k = 0, \pm 1, \pm 2, \ldots \tag{9}$$

where k is integer, $\zeta = \sqrt{-1}$, and:

$$\breve{u}_k(t) = \frac{1}{2\pi} \int_0^{2\pi} u(x,t) e^{-\zeta k x}\, dx, \qquad k = 0, \pm 1, \pm 2, \ldots \tag{10}$$

are the Fourier coefficients of u for different values of k. Equation (10) is also called the Fourier transform of u while Eq. (9) is the inverse Fourier transform relation.

Let the source term $f(x, t)$ and the kernel function with the form below, be also complex-valued functions defined over the periodic domain T.

$$\mu(x) = \begin{cases} \text{even function} & |x| \le \delta \\ 0 & |x| > \delta \end{cases} \tag{11}$$

Then, the PD diffusion equation over the periodic domain T is:

$$\frac{\partial u}{\partial t} = \nu(\mu *_{\mathrm{T}} u - \beta u) + f \tag{12}$$

where $(*_{\mathrm{T}})$ denotes the "circular convolution" integral (aka "cyclic" or "periodic convolution") [73, 74]:

$$\mu *_{\mathrm{T}} u = \int_{\mathrm{T}} \mu(x - \hat{x}) u(\hat{x}, t)\, d\hat{x} \tag{13}$$

We approximate $u(x,t)$ by the *truncated (finite) Fourier series* of u:

$$u^N(x,t) = \sum_{k=-N/2}^{+N/2-1} \breve{u}_k(t)\, e^{\zeta k x} \tag{14}$$

Based on the finite Fourier series approximation, two similar, but not necessarily identical, numerical schemes can be used for solving Eq. (12). One method is the *Fourier-Galerkin* method [75] in which the following weak form is solved:

$$\int_0^{2\pi} \left[\frac{\partial u^N}{\partial t} - \nu(\mu^N *_{\mathrm{T}} u^N) + \nu\beta u^N - f^N \right] e^{-\zeta k x} dx = 0 \quad \text{for each } k = -\frac{N}{2}, \ldots, \frac{N}{2} - 1 \tag{15}$$

Here μ^N and f^N are the finite Fourier series approximations for μ and f. The integration on each term in Eq. (15) is the Fourier transform of that term. Equation (15) is then equivalent to:

$$\frac{d\breve{u}_k}{dt} - 2\pi\nu\breve{\mu}_k\breve{u}_k + \nu\beta\breve{u}_k - \breve{f}_k = 0 \quad \text{for each } k = -\frac{N}{2}, \ldots, \frac{N}{2} - 1 \tag{16}$$

We observe that the circular convolution is transformed into a product operation of Fourier coefficients. In the Fourier-Galerkin method the ODE in Eq. (16) is solved for the Fourier coefficients of u^N. The solution can be transformed to the physical space with the inverse relation given by Eq. (14).

Another approach is the *Fourier Collocation* method [75] which is the one we will use in the present study. This method focuses on the solution in the physical space. The approximated solution in Eq. (14) is represented by its values at grid points $x_i = i\Delta x$, with $\Delta x = \frac{2\pi}{N}$ and $i \in \{0, \ldots, N-1\}$. In this method, $u^N(x, t)$ satisfies the strong form below at the collocation points x_i:

$$\frac{\partial u_i^N}{\partial t} - \nu\left(\mu_i^N *_{\mathrm{T}} u_i^N\right) + \nu\beta u_i^N - f_i^N = 0 \tag{17}$$

Since μ and u are approximated by finite Fourier series, the circular convolution can be evaluated by the inverse transform of the product of Fourier coefficients according to the convolution theorem [74]:

$$\mu^N *_{\mathrm{T}} u^N = \mathcal{F}^{-1}\left(2\pi\breve{\mu}_k\breve{u}_k\right) \tag{18}$$

where $\mathcal{F}^{-1}$ refers to the inverse Fourier transform operation.

For practical applications of this method, a discrete-level operation is required to compute the Fourier transform and its inverse. The obvious choice is the discrete Fourier transform (DFT) [75]:

$$\widetilde{u}_k(t) = \frac{1}{N}\sum_{i=0}^{N-1} u^N(x_i, t)e^{-\zeta kx_i} \tag{19}$$

and its inverse relation (iDFT)

$$u^N(x_i, t) = \sum_{k=-N/2}^{N/2-1} \widetilde{u}_k(t)e^{\zeta kx_i} \tag{20}$$

Note that $\widetilde{u}_k$ are approximations to the exact Fourier coefficients $\breve{u}_k$.

Employing DFT, the Fourier Galerkin method yields to:

$$\frac{d\widetilde{u}_k}{dt} - \nu\left(\widetilde{\mu^N *_{\mathrm{T}} u^N}\right) + \nu\beta\widetilde{u}_k - \widetilde{f}_k = 0 \tag{21}$$

By the convolution theorem for DFT [73] we obtain:

$$\frac{d\widetilde{u}_k}{dt} = \nu\widetilde{\mu}_k\widetilde{u}_k\Delta x - \nu\beta\widetilde{u}_k + \widetilde{f}_k \tag{22}$$

Using DFT and iDFT for transformation, the Fourier Collocation method in Eq. (17) becomes:

$$\frac{\partial u_i^N}{\partial t} = \nu F_{\boldsymbol{D}}^{-1}\left(\widetilde{\mu}_k\widetilde{u}_k\Delta x\right) - \nu\beta u_i^N + f_i^N \tag{23}$$

where F_D^{-1} denotes the inverse DFT. Let S denote the arc length of T (in our case $S = 2\pi$). If the periodic domain of computation is not $[0, S)$, i.e., it does not start at the origin at its left end, for example if it is $[-\frac{S}{2}, \frac{S}{2})$, then the kernel function may need to be shifted depending on the DFT solver (see Appendix 1).

The dominant computational cost in both methods is computing the DFT and its inverse, which are $O(N \log N)$ operations via FFT algorithms [43, 44]. This is a significant improvement over the $O(N^2)$ cost for the meshfree collocation with one-point Gaussian quadrature or the FE methods used for PD problems. The extension of the spectral method to higher dimension is straightforward.

The above scheme works only for problems with periodic boundary conditions. We propose a penalization scheme that will allow us to apply spectral methods to general PD models with non-periodic boundary conditions in the next section.

3.2 Volume Penalization

We employ the volume penalization (VP) technique developed for local problems in [54, 58], to impose arbitrary volume constraints in a general PD problem.

In this method, the one-dimensional domain Ω is extended by δ at both ends as the constrained volume (Γ) to apply the nonlocal boundary conditions. The idea in the VP scheme is to consider periodicity for this extended domain, i.e., $T = \Omega \cup \Gamma$, and penalize the solution in the constrained domain to maintain the desired constraint values (see Fig. 4).

The PD diffusion equation is extended by adding a penalization term, which is zero on Ω, but takes large values on Γ:

$$\frac{\partial u_\varepsilon(x, t)}{\partial t} = \nu \mathcal{L}_\delta u_\varepsilon(x, t) + f(x, t) - \frac{\chi(x, t)}{\varepsilon} [u_\varepsilon(x, t) - u_\Gamma(x, t)] \tag{24}$$

In this equation ε is a small number called here *the penalization factor*, u_ε is the solution to the penalized PD diffusion equation, $u_\Gamma(x, t)$ is the volume constraint value at point $x \in \Gamma$ and time t, and $\chi(x, t)$ is the following mask function:

$$\chi(x, t) = \begin{cases} 1 & x \in \Gamma \\ 0 & x \in \Omega \end{cases} \tag{25}$$

For sufficiently small ε, the penalization term dominates on Γ:

$$\nu \mathcal{L}_\delta u_\varepsilon(x, t) + f(x, t) \ll \frac{1}{\varepsilon} [u_\varepsilon(x, t) - u_\Gamma(x, t)], \tag{26}$$

leading to:

$$\frac{\partial u_\varepsilon(x, t)}{\partial t} \cong -\frac{1}{\varepsilon} [u_\varepsilon(x, t) - u_\Gamma(x, t)] \quad \text{on } x \in \Gamma. \tag{27}$$

Accordingly, this penalization term enforces an exponential decay for u_ε to u_Γ over the constrained domain. This effectively enforces the desired local boundary condition on $\partial\Omega$ if $u_\Gamma(x, t)$ is assigned via the scheme described in Section 2. Discussion on convergence of u_ε to u as ε goes to zero is provided in Section 6.

To apply the spectral method, u_ε is approximated with the finite Fourier series u_ε^N on the periodic domain (T). To avoid complexity in notation, let $y = u_\varepsilon^N$. The spatially discretized

version of Eq. (24) in 1D for using the *boundary-adapted spectral method* (*BASM*) is:

$$\frac{\partial y_i^n}{\partial t} = \nu F_D^{-1}\left(\tilde{\mu}_k^n \tilde{y}_k^n \Delta x\right) - \nu \beta y_i^n + f_i^n - \frac{\chi_i}{\varepsilon}\left(y_i^n - y_{\Gamma,i}^n\right) \tag{28}$$

where the superscript n refers to nth time step. A convergence study with respect to the spatial discretization size is provided in Section 6.

Any applicable temporal integration scheme may be used to now solve the first-order ODE in Eq. (29), and update the solution at each time step. With the Forward Euler method, for example, we have:

$$y_i^{n+1} \approx y_i^n + \Delta t \frac{dy_i^n}{dt} \tag{29}$$

where Δt is the time step. The stability restriction on the time step size for this explicit method is derived in the next section.

Note that although in this study the penalized region is taken to be identical to the constrained volume (Γ), it is possible to consider decoupling of the δ-thick volume constraint and the penalization domain, where Γ is a subdomain of the penalized region. Indeed, this would be necessary in the case of non-rectangular domains in higher dimensions. The decoupling seems also relevant if one wishes to study the behavior of solutions when δ approaches zero in the limit, or to study the influence of the size of the penalized region. However, for the sake of simplicity, we take the horizon size and penalization thickness to be identical in the present work.

4 Stability Analysis

Here we follow the stability analysis in [33] to find the restriction on time steps for the BASM with VP using the explicit Euler time integration scheme. It can be shown that Eq. (29) in the physical space is algebraically equivalent to:

$$\frac{dy_i^n}{dt} = \nu \sum_{j=0}^{N-1} \mu_{i-j} y_j^n \Delta x - \nu \beta y_i^n + f_i^n - \frac{\chi_i}{\varepsilon}\left(y_i^n - y_{\Gamma,i}^n\right) \tag{30}$$

where $\mu_{i-j} = \mu(x_i - x_j)$. Note that the term in the summation above is zero for all $x_j \notin [x_i - \delta, x_i + \delta]$. Although similar, the discretized volume integral in Eq. (30) is not identical to one-point Gaussian quadrature used in the meshfree method. Functions are approximated with the truncated Fourier series, which is not the case in the conventional meshfree method.
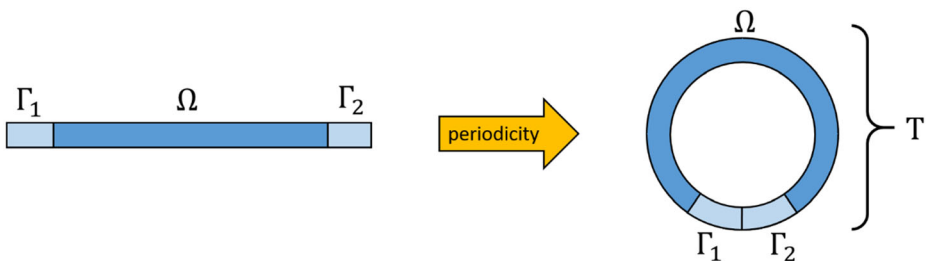

Fig. 4 Extension of 1D peridynamic non-periodic domain ($\Omega \cup \Gamma$) to the periodic domain T used in spectral method with volume penalization

With Forward Euler (first-order explicit) temporal integration, Eq. (30) becomes:

$$\frac{y_i^{n+1}-y_i^n}{\Delta t} = \nu \sum_j \mu_{i-j} y_j^n \Delta x - \nu \beta y_i^n + f_i^n - \frac{\chi_i}{\varepsilon}\left(y_i^n - y_{\Gamma,i}^n\right) \tag{31}$$

Take:

$$y_i^n = \lambda^n e^{\zeta k x_i} \tag{32}$$

where λ is a complex number. Substituting Eq. (32) to Eq. (31), results in:

$$\frac{\lambda^{n+1}-\lambda^n}{\Delta t} e^{\zeta k x_i} = \nu \sum_j \mu_{i-j} \lambda^n e^{\zeta k x_j} \Delta x - \nu \beta \lambda^n e^{\zeta k x_i} + f_i^n - \frac{\chi_i}{\varepsilon}\left(\lambda^n e^{\zeta k x_i} - u_{\Gamma,i}^n\right) \tag{33}$$

For simplicity, let $u_{\Gamma,i}^n = 0$, $f_i^n = 0$, and $\rho = \frac{\lambda^{n+1}}{\lambda^n}$ for every i and n, then:

$$\frac{\rho-1}{\Delta t} = \nu \sum_j \mu_{i-j} e^{\zeta k (x_j - x_i)} \Delta x - \nu \beta - \frac{\chi_i}{\varepsilon} \tag{34}$$

Since $\mu_{i-j} = \mu_{j-i}$, let $p = j - i$, and $x_p = x_j - x_i$, we obtain:

$$\frac{\rho-1}{\Delta t} = \nu \sum_p \mu_p e^{\zeta k x_p} \Delta x - \nu \beta - \frac{\chi_i}{\varepsilon} \tag{35}$$

If $m = \frac{\delta}{\Delta x}$ is integer, then, since $\mu_p = \mu_{-p}$ and $x_{-p} = -x_p$:

$$\sum_{p=-m}^{+m} \mu_p e^{\zeta k x_p} \Delta x = \sum_{p=1}^{m}\left(\mu_p e^{\zeta k x_p}\Delta x + \mu_{-p} e^{\zeta k x_{-p}}\Delta x\right) + \mu_0 \Delta x = 2\sum_{p=0}^{m}\mu_p \cos(k x_p)\Delta x$$

$$= \sum_{p=-m}^{m}\mu_p \cos(k x_p)\Delta x \tag{36}$$

Substituting Eq. (39) into Eq. (38) results in:

$$\frac{\rho-1}{\Delta t} = \nu\left(\sum_{p=-m}^{m}\mu_p \cos(k x_p)\Delta x - \beta\right) - \frac{\chi_i}{\varepsilon} \tag{37}$$

Define M:

$$M = \nu\left(\sum_{p=-m}^{m}\mu_p \cos(k x_p)\Delta x - \beta\right) \tag{38}$$

Then:

$$\rho = \left(M - \frac{\chi_i}{\varepsilon}\right)\Delta t + 1 \tag{39}$$

To maintain stability, we seek Δt such that $|\rho| \leq 1$. Therefore:

$$\left|\left(M - \frac{\chi_i}{\varepsilon}\right)\Delta t + 1\right| \leq 1 \tag{40}$$

or,

$$-1 \leq \left(M - \frac{\chi_i}{\varepsilon}\right)\Delta t + 1 \leq 1 \tag{41}$$

or equivalently:

$$0 \leq \left(\frac{\chi_i}{\varepsilon} - M\right)\Delta t \leq 2 \tag{42}$$

In order to satisfy the left inequality in Eq. (42), since χ_i is either 0 or 1, and that ε and Δt are positive quantities, we need $M \leq 0$. According to Eq. (38), this imposes the following condition on $\mu(x)$:

$$\sum_{p=-m}^{m} \mu_p \cos(kx_p)\Delta x \leq \beta = \int_{-\delta}^{\delta} \mu(x)\mathrm{d}x \tag{43}$$

This condition holds for sufficiently small Δx, since:

$$\int_{-\delta}^{\delta} \mu(x)\cos(kx)\mathrm{d}x \leq \int_{-\delta}^{\delta} \mu(x)\mathrm{d}x \tag{44}$$

Most kernel functions in use satisfy the requirement in Eq. (48).

The inequality in Eq. (44) also requires:

$$\Delta t \leq \frac{2}{\dfrac{\chi_i}{\varepsilon} - M} \tag{45}$$

From Eqs. (38) and (48):

$$-M \leq 2\nu\beta \tag{46}$$

According to Eqs. (45) and (46), and that χ_i is either 0 or 1, the following restriction on Δt for stable solution is suggested:

$$\Delta t \leq \frac{2}{\dfrac{1}{\varepsilon} + 2\nu\beta}. \tag{47}$$

Even if the restriction above is obtained assuming zero values for u_Γ and f, we find that it is also sufficient for obtaining stable results for the examples shown in Section 5, with nonzero u_Γ and f.

From Eq. (47), we see that penalization puts a stronger restriction on the time step compared with the condition found with the conventional meshfree method [69]. However, the cost due to the increased number of time steps is likely to be overcome by the gains in the complexity order (in terms of node number) when computing the convolution integral with FFT. Note that the increased number time steps does affect the complexity order, since according to Eq. (47), the time step size does not depend on N.

We also note that, even though our method is purely explicit, we do not have the standard CFL stability constraint that appears in local problems; namely, $\Delta t_{\max} \propto (\Delta x^2 / \nu)$. Indeed, $\Delta t_{\max}$ depends on the size of the horizon size (implicitly through β), but does not depend at all on Δx (see also [33]). While this may seem surprising at first, as it allows for extremely high spatial resolutions to be stable with relatively low

temporal resolutions (in contrast to local problems), in fact it is expected due to the convolution structure of the nonlocal equation. Namely, at a given spatial location x, the convolution integral incorporates all information within a ball of δ, which is then propagated forward in time. Thus, the expected CFL constraint for nonlocal problems depends on δ, which is essentially what we see in Eq. (47).

5 Example Problems and Discussion

We now compare the performance of the PD spectral method with the regular integration (one-point Gaussian quadrature) of the convolution integral in the PD Laplacian. Then, we analyze two one-dimensional nonlocal diffusion problems to demonstrate the capability of the BASM introduced. The first problem has local Dirichlet boundary conditions at both ends, while the second has local Neumann boundary conditions at both ends.

For these examples we need to select a kernel function $\mu(x)$. According to [76], one possible choice for the kernel function is of the form:

$$\mu(\boldsymbol{x}) = \frac{(4-\alpha)(3-\alpha)}{\delta^{(3-\alpha)}} \left(1 - \frac{|x|}{\delta}\right) \frac{1}{|x|^\alpha} \tag{48}$$

where α can take values 0, 1, and 2, for example (for details see [76]). For the case $\alpha = 0$, we have:

$$\mu(x) = \frac{12}{\delta^3} \left(1 - \frac{|x|}{\delta}\right) \tag{49}$$

Chen and Bobaru [76] showed that a constructive approach to a peridynamic kernel leads to the choice of $\alpha = 2$. Here, however, we choose $\alpha = 0$ for simplicity and to avoid the singularity when calculating $\beta = \int_{H_0} \mu(x) dx$. For the case $\alpha = 0$, this integral is $\frac{12}{\delta^2}$. For the other values of α, β can be calculated using the Cauchy principal value [77].

5.1 Efficiency of the Peridynamic Spectral Method

Here we compute $\mathcal{L}_\delta u$ for $u = \sin(\pi x)$ with $\delta = 0.2$ in $x \in [-1, 1]$ via two methods: the direct numerical integration using one-point Gaussian quadrature:

$$(\mathcal{L}_\delta u)_i = \sum_{j=i-\text{round}(\delta/\Delta x)}^{i+\text{round}(\delta/\Delta x)} \mu_{i-j} u_j \Delta x - \beta \tag{50}$$

and the spectral method:

$$(\mathcal{L}_\delta u)_i = F_{\boldsymbol{D}}^{-1}\left(\widetilde{\mu}_k \widetilde{u}_k \Delta x\right) - \beta \tag{51}$$

The kernel function μ is the one defined by Eq. (49), and therefore $\beta = \frac{12}{\delta^2}$.

$\mathcal{L}_\delta u$ is computed using both methods for several discretization sizes, with N varying between 2^8 to 2^{20}. Computations are performed using *MATLAB 2018a* on a Dell-Precision

Table 1 Comparison of run-times between the one-point Gaussian quadrature and the spectral method in calculating the peridynamic Laplacian

N (number of nodes)	Gaussian quadrature time (s)	Spectral method time (s)
$2^8 = 256$	1.79e−4	2.11e−5
$2^{12} = 4096$	5.03e−2	1.63e−4
$2^{16} = 65,536$	1.07e+1	5.04e−3
$2^{20} = 1,048,576$	3.00e+3 (50 min)	6.73e−2 (67 ms)

T7810 workstation PC, with twenty logical Intel(R) Xeon(R) CPU E5-2687 W v3 @3.10 GHz processors, and 64 GB of installed memory. The computational times for each method to calculate $\mathcal{L}_\delta u$ for various discretization sizes are provided in Table 1.

As observed, the time for one-point Gaussian quadrature is $O(N^2)$, while the spectral method performs even more efficient than $O(N \log N)$. The reason for the over-performance of the spectral method may be due to the efficient FFT solver in MATLAB, which uses optimized algorithms with respect to data size and structure.

5.2 Transient Diffusion with Dirichlet Boundary Conditions

We now solve an example of PD transient diffusion problem with local Dirichlet BCs (inhomogeneous), using the BASM, and compare the numerical solution with the analytical solution. Consider, for example:

$$u(x, t) = \frac{2x}{L} + e^{-\nu t} \sin\left(\frac{2\pi x}{L}\right) \tag{52}$$

The function in Eq. (52) is the exact solution to the following nonlocal diffusion problem over the domain $\Omega = \left[-\frac{L}{2}, \frac{L}{2}\right]$:

$$\frac{\partial u(x, t)}{\partial t} = \nu \mathcal{L}_\delta u(x, t) + f(x, t), \tag{53}$$

with

$$f(x, t) = \nu \left\{ \frac{6L^2}{\delta^4 \pi^2} \left[\cos\left(\frac{2\pi\delta}{L}\right) - 1 \right] + \frac{12}{\delta^2} - 1 \right\} e^{-\nu t} \sin\left(\frac{2\pi x}{L}\right) \tag{54}$$

the initial condition:

$$u(x, 0) = \frac{2x}{L} + \sin\left(\frac{2\pi x}{L}\right) \tag{55}$$

and the local Dirichlet boundary conditions:

$$u\left(-\frac{L}{2}, t\right) = -1 \tag{56}$$

$$u\left(\frac{L}{2}, t\right) = 1 \tag{57}$$

The manufactured solution $u(x, t)$ in Eq. (52) has a special property: with the fictitious nodes scheme described in Section 2, the values of u in $\left[-\frac{L}{2}-\delta, \ -\frac{L}{2}\right)$ and $\left(\frac{L}{2}, \ \frac{L}{2}+\delta\right]$, satisfy the volume constraint relationship in Eq. (6). This property then makes it easier to find the $f(x, t)$ above. Without this property, one can still find $f(x, t)$ analytically, but as a relatively more complex piecewise function.

To solve this problem with the proposed method, we select $L = 2$, $\nu = 0.2$, $\delta = 0.2$, and the total diffusion time $t_{max} = 15$. The computational domain is then extended to $T = \Omega \cup \Gamma : \left[-\frac{L}{2}-\delta, \frac{L}{2}+\delta\right) = [-2.2, 2.2)$, with $[-2.2, -2)$ and $(2, 2.2)$ being the constrained domains Γ_1 and Γ_2 respectively. Note that the computational domain interval does not include $x = 2.2$ due to the periodicity of the spectral method that mandates $x = 2.2$ be identical to $x = -2.2$. Choosing the number of spatial nodes to be a power of two ($N = 2^P$) has certain benefits in parallelization of FFT algorithms [44]. The extended domain $[-2.2, 2.2)$ is discretized with $N = 2^9$ nodes. The time step and penalization factor are selected as $\Delta t = 5 \times 10^{-4}$ and $= 5 \times 10^{-4}$, respectively. The algorithm for the implementation of the proposed method is provided in the Appendix 1, and the corresponding MATLAB code is provided in Online Resource 1. According to the fictitious nodes scheme described in Section 2, volume constraint values on Γ are calculated explicitly from Eqs. (58) and (59), using the solution on Ω at the previous time step. For $x \in \Gamma_1 : \left[-\frac{L}{2}-\delta, -\frac{L}{2}\right)$:

$$y_{\Gamma 1}\left(x_i, t^{n+1}\right) = 2u_{b1} - y(2\delta - x_i, t^n), \tag{58}$$

where u_{b1} is the Dirichlet BC value given in Eq. (56), and y is u_ε^N: the numerical solution using the BAS method with VP. For $x \in \Gamma_2 : \left(\frac{L}{2}, \frac{L}{2}+\delta\right)$, the equation below applies the boundary condition:

$$y_{\Gamma 2}\left(x_i, t^{n+1}\right) = 2u_{b2} - y(2L + 2\delta - x_i, t^n), \tag{59}$$

where u_{b2} is the BC value given in Eq. (57). Note that the volume constraints can be applied implicitly as well by replacing t^n with t^{n+1} in Eqs. (58) and (59), where one need to iterate until y_Γ^{n+1} converges.

Figure 5 shows the time snapshots of the nonlocal diffusion process. We observe the excellent match with the analytical nonlocal solution for this non-periodic problem.

The absolute error distribution, normalized by the infinity norm of the initial data function $\left(\frac{\left|u-u_\varepsilon^N\right|}{\|u_0\|_\infty}\right)$ is plotted in Fig. 6. We observe the rise and decay of the error in time, in the interior
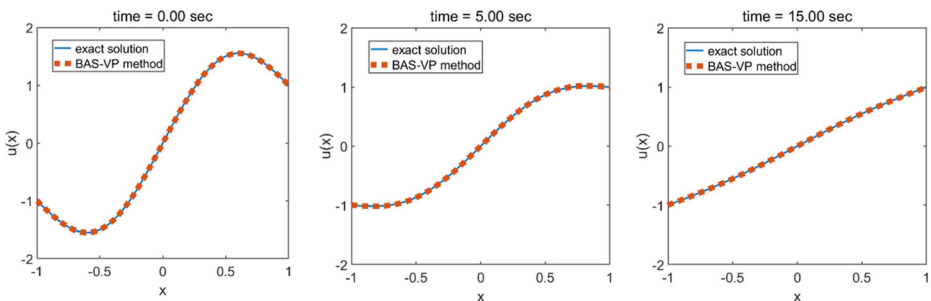

Fig. 5 Comparison between the analytical solution of a nonlocal 1D diffusion process, with non-periodic (Dirichlet) boundary conditions, and the solution obtained by the peridynamic spectral method with volume penalization
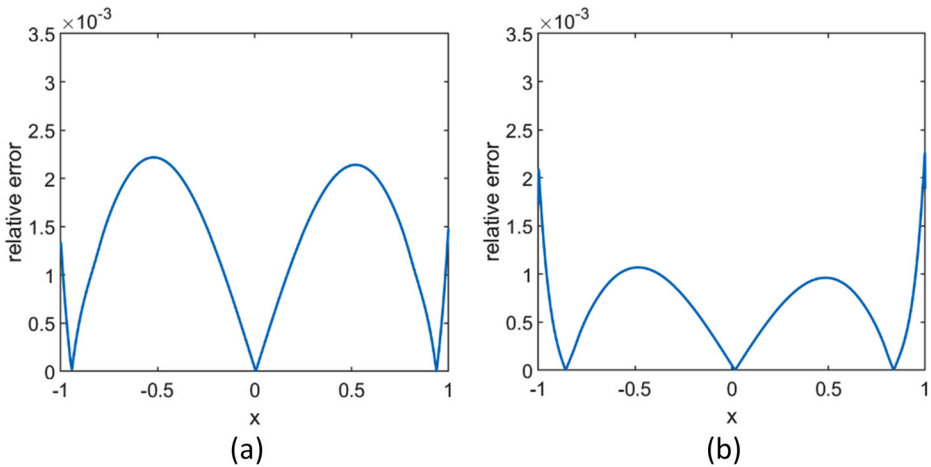
Fig. 6 Time snapshots of the relative error in 1D nonlocal diffusion with non-periodic (Dirichlet) boundary conditions using the peridynamic spectral method with volume penalization. **a** $t = 5$; **b** $t = 15$

region of the domain Ω, while the error near the boundaries rises and approaches to permanent amount (see Video 1).

The maximum relative error ($\frac{\|u - u_\varepsilon^N\|_\infty}{\|u_0\|_\infty}$) is plotted versus diffusion time in Fig. 7. The slope discontinuity in this plot can be understood by observing the behavior in Video 1: the location of the maximum relative error switches to the boundaries, as time progresses.

This plot suggests that the observed error time-evolution consists of two periods: at first, the error in the domain interior dominates, while later the error near the boundaries becomes more important. Our parametric studies in Appendix 2 show that the decaying error on the interior originates from the spatial discretization and is reduced with grid refinement. The error near the boundaries, however, depends of the penalization factor and is reduced by selecting a smaller ε. Convergence studies for the total error in terms of discretization size and penalization parameter are given in Section 6.

While the main benefit of the BASM for PD is its low complexity compared with the alternative discretization methods of the nonlocal equations (the meshfree method or the FEM), wide availability of commercial multithreaded or GPU-enhanced FFT solvers allows us to

Fig. 7 Variation of the maximum relative error in time for the 1D nonlocal diffusion example with non-periodic (Dirichlet) boundary conditions, using the peridynamic spectral method with volume penalization
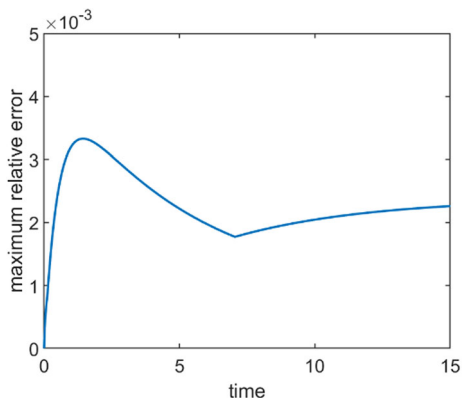
further increase computational efficiency minimal additional coding effort. For example, with minimal modification of the code (see the Online Resource 1), we used MATLAB built-in FFT solver on a *NVIDIA Quadro K2200* GPU to further accelerate computations for the problem described in this section, when the problem size is large. In Table 2 we show the computational time of the BASM with and without GPU, and also the time for the meshfree method.

Note that due to the stricter stability criterion caused by the penalization, the BASM used 3×10^4 time steps to simulate the 15 s of diffusion in the example above, while the meshfree method used only 900 steps. Nevertheless, the BAS method shows orders of magnitude gains in efficiency compared with the one-point Gaussian quadrature.

For $N = 2^{16}$ or coarser spatial discretizations, GPU-based computations do not improve the run-time compared with the CPU-only case, which is expected due to the time consumed by data transfer onto the GPU. When the problem size is larger, however, minimal changes to a few lines of code lead to significant speed-up (see Table 2). Note also that MATLAB's built-in fft function is multithreaded in 2D or higher dimensions, but not in 1D.

5.3 Transient diffusion with Neumann Boundary Conditions

To demonstrate the capability of the proposed method in solving PD problems with arbitrary boundary conditions, we now discuss an example with Neumann BCs. Consider the function:

$$u(x,t) = \frac{2x}{L} + e^{-\nu t}\cos\left(\frac{2\pi x}{L}\right), \tag{60}$$

the exact solution for the nonlocal diffusion equation in Eq. (53) on the interval $\left[-\frac{L}{2}, \frac{L}{2}\right]$, with

$$f(x,t) = \nu\left\{\frac{6L^2}{\delta^4\pi^2}\left[\cos\left(\frac{2\pi\delta}{L}\right)-1\right] + \frac{12}{\delta^2}-1\right\}e^{-\nu t}\cos\left(\frac{2\pi x}{L}\right), \tag{61}$$

initial condition

$$u(x,0) = \frac{2x}{L} + \cos\left(\frac{2\pi x}{L}\right), \tag{62}$$

and local Neumann BCs:

$$\frac{\partial u}{\partial x}\left(-\frac{L}{2}, t\right) = 1 \tag{63}$$

$$\frac{\partial u}{\partial x}\left(\frac{L}{2}, t\right) = 1. \tag{64}$$

Similar to the previous example for Dirichlet BC, the manufactured solution in Eq. (60) satisfies the volume constraint relationship in Eq. (8) when $x \in \Gamma_1$ or Γ_2.

For this problem, L, δ, ν, and $t_{\max}$, are the same as in the previous example in Section 5.1. We use the explicit implementation of the fictitious nodes scheme for applying the volume

Table 2 Comparison of run-times for the transient diffusion problem between the BASM (with and without GPU), and the meshfree method with Gaussian quadrature (GQ)

N (number of nodes)	Meshfree with GQ	BASM on CPU	BASM on CPU+GPU
$2^{16} = 65,536$	92 min	81.2 s	126 s
$2^{20} = 1,048,576$	17 days	28 min	12 min
$2^{24} = 16,777,216$	12 years (estimated)	9.5 h	3.2 h

constraints corresponding to Neumann BC (see Eq. (8)). For $x \in \Gamma_1 : \left[-\frac{L}{2} - \delta, -\frac{L}{2} \right)$ we get:

$$y_{\Gamma 1}\left(x_i, t^{n+1}\right) = -2q_{b1}(\delta - x_i) + y(2\delta - x_i, t^n), \tag{65}$$

while for $x \in \Gamma_2 : \left(\frac{L}{2}, \frac{L}{2} + \delta \right)$, we have:

$$y_{\Gamma 2}\left(x_i, t^{n+1}\right) = -2q_{b2} + y\left(2L + 2\delta - x_i, t^n \right) \tag{66}$$

Values for both q_{b1} and q_{b2} are 1 according to Eqs. (63) and (64). For the numerical solution, N, Δt, and ε are the same as in the previous example.

Figure 8 shows the evolution in time of the numerical solution y in comparison with the exact nonlocal solution u. The results support the fact that the BAS method is capable of solving peridynamic problems with arbitrary boundary conditions.

As mentioned in the introduction section, volume penalization is only one way to use Fourier spectral methods on irregular domains with arbitrary boundary conditions. Alternative BAS methods for peridynamics can be constructed, if one employs other boundary adapting schemes such as the smoothed boundary method [55, 56].

6 Convergence

In this section we first provide a brief background on error estimates for the volume penalization method, and then present convergence studies with respect to the penalization and spatial discretization for the example problem shown in Section 5.2.

Angot et al. [58] proved that the solution of Navier-Stokes equation with the volume penalization in a periodic domain converges to the solution of Navier-Stokes equation with the
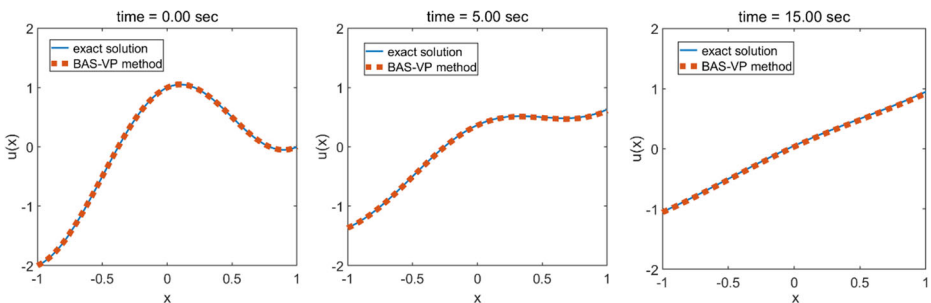

Fig. 8 Comparison between the analytical solution of a nonlocal 1D diffusion process, with non-periodic Neumann boundary conditions, and the solution obtained by the peridynamic spectral method with volume penalization

proper exact boundary conditions, as ε goes to zero. The error in the main domain for that case is shown to be at most of the $O(\varepsilon^{3/4})$. In the case of the classical diffusion equation, Kevlahan and Ghidaglia [54] showed for a specific problem that the error between the penalized periodic solution and the exact solution to the diffusion equation with non-periodic boundary conditions is at most $O(\varepsilon^{1/2})$. They observed that the computed error is $O(\varepsilon)$.

While a rigorous mathematical convergence analysis and error estimate for nonlocal diffusion equation with penalization and spectral method would be ideal, in this study we only provide some numerical results. The complete theoretical analysis is left for the future. We perform convergence studies on the example with two Dirichlet BCs discussed in Section 5.2.

First we study the convergence of the penalized periodic solution u_ε^N (the solution to Eq. (24)), to the exact solution (Eq. (52)) of the un-penalized diffusion equation with Dirichlet BC. To this aim, we need to choose a relatively large N, and relatively small time step and keep them fixed while decreasing ε in each test. This makes the discretization and temporal integration errors minor compared with the penalization error which we want to investigate. We need to also choose a time span to approach the steady state where according to the observations in Figs. 6 and 7 permanent penalization error is dominated and remains relatively constant. The selected parameters for this convergence study are $N = 2^{15}$, $\Delta t = 1.97 \times 10^{-4}$, and $t_{\max} = 30$, while ε^{-1} value varies for each test. Δt satisfies Eq. (47) restriction with the smallest penalization factor used in this convergence study ($\varepsilon = 1 \times 10^{-4}$). Figure 9 shows the relative error versus ε^{-1} for each test.

The results show that the penalization error varies with $O(\varepsilon)$, which is consistent with observations for the penalized classical diffusion equation [59].

To observe the convergence behavior with respect to spatial discretization size, we compare the maximum error in the whole time span for various N values, while keeping constant the relatively small values of Δt and ε. To this aim, we obtained the error $\max\limits_{0 < t < t_{\max}} \dfrac{\left\| u - u_\varepsilon^N \right\|_\infty}{\left\| u_0 \right\|_\infty}$, with respect to different N values in five tests with $\varepsilon = 5 \times 10^{-6}$, and $\Delta t = 9.99 \times 10^{-6}$. Again, Δt satisfies the stability condition given in Eq. (47). Results are plotted in Fig. 10.

Fig. 9 Convergence study in terms of penalization factor for the peridynamic spectral method with volume penalization on the problem with Dirichlet boundary conditions shown in Section 5.2
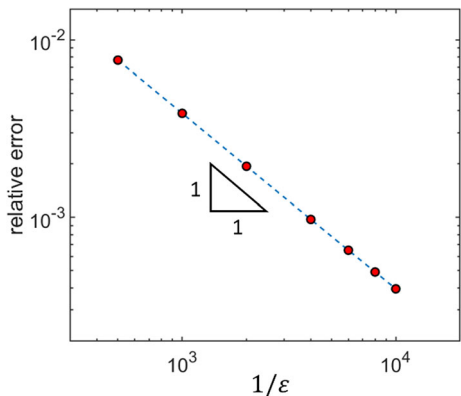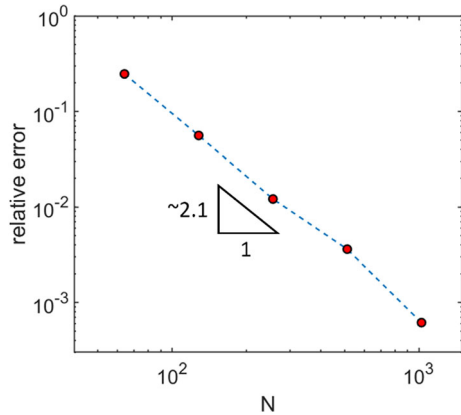
Fig. 10 Convergence study with respect to the spatial discretization size for the spectral method with volume penalization on the problem with Dirichlet boundary conditions shown in Section 5.2

As observed, the spatial convergence rate of peridynamic BASM is $O(\Delta x^2)$ for this example problem. This is similar to meshfree-collocation method with one-point Gaussian quadrature [33].

Note that the all the comparisons of the solutions with exact solution for obtaining errors are considered within the domain of interest $\Omega = T\backslash\Gamma$ which disregards the solution values on the penalized region Γ.

The general error of the peridynamic BASM is bounded by the summation of the penalization error, spatial discretization errors (finite Fourier series approximation and DFT), and the explicit time integration error which for Forward Euler is known to be $O(\Delta t)$.

For the presented example with two Dirichlet BCs, the error of the introduced method appears to be bounded by $O(\varepsilon) + O(\Delta x^2) + O(\Delta t)$.

7 Conclusions

In this study, we introduced a boundary-adapted spectral method (BASM) for peridynamic (PD) transient diffusion problems with arbitrary boundary conditions. The spectral approach transforms the convolution integral into a multiplication in the Fourier space, resulting in computations that scale as $O(N \log N)$. We demonstrated the efficiency of this method by comparing it with the commonly used one-point Gaussian quadrature method for spatial integration in a peridynamic model. In 1D, a transient diffusion problem with roughly sixteen million nodes is solved in a few hours with the spectral method whereas the one-point Gaussian quadrature approach would require over 12 years (!) to complete. We also showed that using MATLAB's built-in FFT solver on GPU (by performing minimal changes to the code) produces significant speed-ups for the larger scale problems. The source code for this example was provided in Online Resource 1.

A stability analysis for the peridynamic BASM (with the volume-penalization approach) with Forward-Euler time integration for peridynamic transient diffusion

problems suggested that the restriction on the time-step varies linearly with the penalization factor, for a sufficiently large one. We examined the performance of the method introduced for arbitrary boundary conditions with two examples of peridynamic transient diffusion using local Dirichlet and Neumann boundary conditions. We compared our numerical results against exact nonlocal solutions, constructed using the method of manufactured solutions. Our convergence studies show that the error scales linearly with the penalization factor and quadratically with the discretization size. The method can be easily extended to other peridynamic/nonlocal models, in 1D and in higher dimensions.

Appendix 1. Boundary-adapted spectral method implementation for PD diffusion in MATLAB

Here the MATLAB implantation for boundary-adapted spectral method with volume penalization (BASM-VP) is provided. First, note that Eq. (23) can be directly used when the periodic domain of computation is $[0, S)$, meaning the origin locates on the left end of the domain. If the domain of choice is $[b, b + S)$, then the following modified form of Eq. (23) should be used:

$$\frac{du_i^N}{dt} = \nu F_D^{-1}\left(\widetilde{\mu^s}_k \widetilde{u}_k \Delta x\right) - \nu\beta u_i^N + f_i^N \tag{67}$$

where $\widetilde{\mu^s}_k$ is the DFT of the shifted kernel function:

$$\mu^s(x) = \mu(x-b) \tag{68}$$

The reason is that the DFT definitions that govern the FFT solvers are based on $[0, S)$ domain. If $b = 0$, then the kernel function does not shift and Eq. (67) becomes identical to Eq. (23).

A MATLAB implementation of the peridynamic BASM with VP for the transient diffusion example in Section 5.2 is as follows:

- Inputs:
- Physical parameters: ν, δ, $f(x, t)$, $\mu(x)$, L, $t_{\max}$
- Initial and boundary conditions: $u(x, 0)$, $u\left(-\frac{L}{2}, 0\right) = u_{b1}$, $u\left(\frac{L}{2}, 0\right) = u_{b2}$
- BASM with VP parameters: N, ε
- Initialization:
- Calculate grid size: $\Delta x = \frac{L+2\delta}{N}$ (length of the extended domain divided by N)
- Calculate time step: Δt from Eq. (47) with ν, ε, and $\mu(x)$
- Discretize the extended domain: $x_i = -\frac{L}{2} - \delta + (i-1)\Delta x$ and $i = 1, 2, \ldots, N$

- Shift the kernel function based on left-end of the extended domain and discretize: $\mu_i^s = \mu\left(x_i + \frac{L}{2} + \delta\right)$
- Discretize the initial condition and the Source term: $y_i^0 = u(x_i, 0)$; $f_i^0 = f(x_i, 0)$;
- Fast Fourier transform μ_i^s and y_i^0: $\widetilde{\mu^s}_k = \mathbf{FFT}\left(\mu_i^s\right)$ and $\widetilde{y^0}_k = \mathbf{FFT}\left(y_i^0\right)$
- Define constrained regions: $\Gamma_1 = x_i \in \left[-\frac{L}{2} - \delta, -\frac{L}{2}\right)$ and $\Gamma_2 = x_i \in \left(\frac{L}{2}, \frac{L}{2} + \delta\right)$
- Define the main domain: $\Omega = x_i \in \left[-\frac{L}{2}, \frac{L}{2}\right]$
- Discretize the mask function: $\chi_i = \chi(x_i)$ from Eq. (25).
- Calculate volume constraints on Γ_1 and Γ_2 from Eq. (58) and (59): $u_{\Gamma 1}(\Gamma_1, 0)$, $u_{\Gamma 2}(\Gamma_2, 0)$

$$\text{Define } y_{\Gamma i}^0 = \begin{cases} Eq. \text{ (58)} & x_i \in \left[-\frac{L}{2} - \delta, -\frac{L}{2}\right) \\ 0 & x_i \in \left[-\frac{L}{2}, \frac{L}{2}\right] \\ Eq.(59) & x_i \in \left(\frac{L}{2}, \frac{L}{2} + \delta\right) \end{cases}$$

- Initialize step counter: $n = 0$
- Initialize time: $t^n = 0$
- Solve the transient diffusion: while $t^n < t_{\max}$
- Update time: $t^{n+1} = t^n + \Delta t$
- Update solution: $y_i^{n+1} = y_i^n + \Delta t\left[\nu\mathbf{FFT^{-1}}\left(\widetilde{\mu^s}_k \widetilde{y^n}_k \Delta x\right) - \nu\beta y_i^n + f_i^n - \frac{\chi_i}{\varepsilon}\left(y_i^n - y_{\Gamma,i}^n\right)\right]$
- Update the source term: $f_i^{n+1} = f_i(x_i, t^{n+1})$
- Update volume constraints: $y_{\Gamma i}^{n+1} = \begin{cases} Eq.(58) & x_i \in \left[-\frac{L}{2} - \delta, -\frac{L}{2}\right) \\ 0 & x_i \in \left[-\frac{L}{2}, \frac{L}{2}\right] \\ Eq.(59) & x_i \in \left(\frac{L}{2}, \frac{L}{2} + \delta\right) \end{cases}$
- Fast Fourier transform y_i^{n+1}: $\widetilde{y^{n+1}}_k = \mathbf{FFT}\left(y_i^{n+1}\right)$
- Update step counter: $n = n + 1$

The algorithm above is for the example with Dirichlet BCs. The corresponding MATLAB code is provided in Online Resource 1. In the case of Neumann BCs Eqs. (58) and (59) are replaced with Eqs. (65) and (66).

Appendix 2. Discretization error versus penalization error in BASM-VP

To obtain a better understanding of error distribution on the domain for the example in Section 5.2, and the evolution of maximum error during the diffusion process (see Figs. 6 and 7), we conducted two more simulations: one simulation with a much smaller ε compared with the test Section 5.2, but the same N, and one simulation with a much larger N compared with that test, but the same ε. The first simulation reveals the error behavior with respect to the discretization, while the second one is focused on the penalization error.

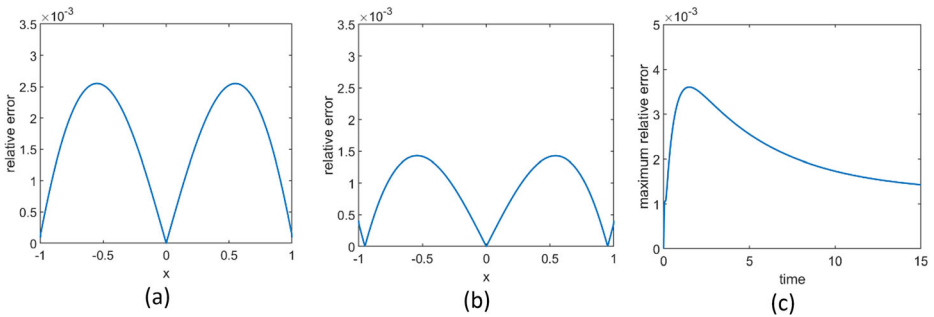Results for the first simulation with $\varepsilon = 5 \times 10^{-6}$, $N = 2^9$ are given in Fig. 11.

Fig. 11 Time snapshots of the relative error dominated by discretization in 1D nonlocal diffusion problem in Section 5.2 at $t = 5$ (**a**), and $t = 15$ (**b**). The time-evolution of the maximum error in (**c**)

The second simulation is performed with $\varepsilon = 5 \times 10^{-4}$ and $N = 2^{15}$. Results are given in Fig. 12.
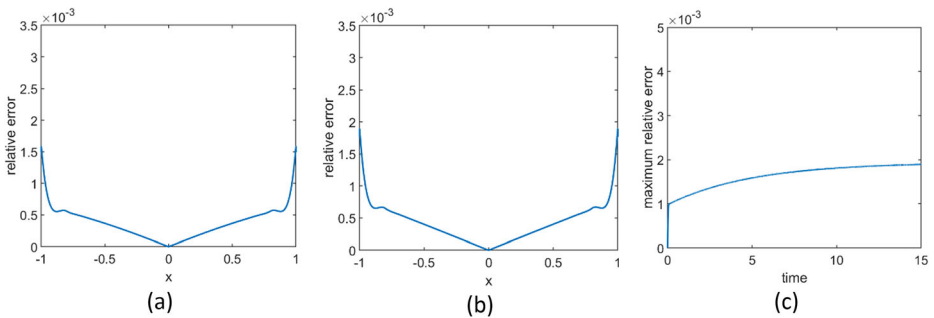

Fig. 12 Time snapshots of the relative error dominated by penalization in 1D nonlocal diffusion problem shown in Section 5.2 at $t = 5$ (**a**), and $t = 15$ (**b**). The time-evolution of maximum error in (**c**)

The discretization error rapidly grows and then decays, while the penalization error grows near the boundaries and approaches a constant value in time. Comparing Figs. 11 and 12 with Figs. 6 and 7 in Section 5.2 (see also video 1) helps us to clearly identify the "mixture" of the penalization and discretization errors in the example corresponding to Figs. 6 and 7.

References

1. Gourley S, So J-H, Wu J (2004) Nonlocality of reaction-diffusion equations induced by delay: biological modeling and nonlinear dynamics. J Math Sci 124(4):5119–5153
2. Mogilner A, Edelstein-Keshet L (1999) A non-local model for a swarm. J Math Biol 38(6):534–570
3. Colombo RM, Garavello M, Lécureux-Mercier M (2012) A class of nonlocal models for pedestrian traffic. Mathematical Models and Methods in Applied Sciences 22(04):1150023
4. Carrillo JA, Fornasier M, Rosado J, Toscani G (2010) Asymptotic flocking dynamics for the kinetic Cucker–Smale model. SIAM J Math Anal 42(1):218–236
5. Cucker F, Smale S (2007) Emergent behavior in flocks. IEEE Trans Autom Control 52(5):852–862
6. Shvydkoy R, Tadmor E (2018) Eulerian dynamics with a commutator forcing III. Fractional diffusion of order 0< α< 1. Physica D: Nonlinear Phen 376:131–137
7. Eringen AC (1972) Linear theory of nonlocal elasticity and dispersion of plane waves. Int J Eng Sci 10(5):425–435

8. Romano G, Barretta R (2017) Stress-driven versus strain-driven nonlocal integral model for elastic nano-beams. Composites Part B 114:184–188
9. Bažant ZP, Jirásek M (2002) Nonlocal integral formulations of plasticity and damage: survey of progress. J Eng Mech 128(11):1119–1149
10. Silling SA (2000) Reformulation of elasticity theory for discontinuities and long-range forces. J Mech Phys Sol 48(1):175–209
11. Bobaru F, Zhang G (2015) Why do cracks branch? A peridynamic investigation of dynamic brittle fracture. Int J Fract 196(1–2):59–98
12. Bažant ZP (1991) Why continuum damage is nonlocal: micromechanics arguments. J Eng Mech 117(5): 1070–1087
13. Bobaru F, Foster JT, Geubelle PH, Silling SA (2016) *Handbook of peridynamic modeling*. CRC Press, Florida
14. Silling SA, Lehoucq R (2010) Peridynamic theory of solid mechanics. In *Advances in Applied Mechanics* (Vol. 44, pp. 73-168). Elsevier, Amsterdam
15. Zhang G, Gazonas GA, Bobaru F (2018) Supershear damage propagation and sub-Rayleigh crack growth from edge-on impact: a peridynamic analysis. Inter J Impact Engin 113:73–87
16. Xu Z, Zhang G, Chen Z, Bobaru F (2018) Elastic vortices and thermally-driven cracks in brittle materials with peridynamics. Int J Fract 209(1–2):203–222
17. Ha YD, Bobaru F (2011) Characteristics of dynamic brittle fracture captured with peridynamics. Eng Fract Mech 78(6):1156–1168
18. Mehrmashhadi J, Tang Y, Zhao X, Xu Z, Pan JJ, Van Le Q et al (2019) The effect of solder joint microstructure on the drop test failure—a peridynamic analysis. IEEE Trans Compon Packag Manuf Technol 9(1):58–71
19. Kamensky D, Behzadinasab M, Foster JT, Bazilevs Y (2019) Peridynamic modeling of frictional contact. J Peridy Nonloc Model 1:107–121. https://doi.org/10.1007/s42102-019-00012-y
20. Zhang G, Le Q, Loghin A, Subramaniyan A, Bobaru F (2016) Validation of a peridynamic model for fatigue cracking. Eng Fract Mech 162:76–94
21. Behzadinasab M, Vogler TJ, Peterson AM, Rahman R, Foster JT (2018) Peridynamics modeling of a shock wave perturbation decay experiment in granular materials with intra-granular fracture. J Dynam Behav Mat 4(4):529–542
22. Chen Z, Niazi S, Zhang G, Bobaru F (2018) Peridynamic functionally graded and porous materials: modeling fracture and damage. In: Voyiadjis G (ed) *Handbook of Nonlocal Continuum Mechanics for Materials and Structures*. Springer International Publishing, Berlin, pp. 1353–1387. https://doi.org/10.1007/978-3-319-22977-5_36-1
23. Chen Z, Niazi S, Bobaru F (2019) A peridynamic model for brittle damage and fracture in porous materials. Int J Rock Mech Min 122:104059
24. Bobaru F, Mehrmashhadi J, Chen Z, Niazi S (2018) Intraply fracture in fiber-reinforced composites: a peridynamic analysis. In *ASC 33rd Annual Technical Conference & 18th US-Japan Conference on Composite Materials, Seattle*, p 9
25. Mehrmashhadi J, Chen Z, Zhao J, Bobaru F (2019) A stochastically homogenized peridynamic model for intraply fracture in fiber-reinforced composites. Compos Sci Technol 182:107770
26. Chen Z, Bobaru F (2015) Peridynamic modeling of pitting corrosion damage. J Mech Phys Sol 78:352–381
27. Jafarzadeh S, Chen Z, Bobaru F (2018) Peridynamic modeling of repassivation in pitting corrosion of stainless steel. Corrosion 74(4):393–414
28. Jafarzadeh S, Chen Z, Bobaru F (2018) Peridynamic modeling of intergranular corrosion damage. J Electrochem Soc 165(7):C362–C374
29. Jafarzadeh S, Chen Z, Zhao J, Bobaru F (2019) Pitting, lacy covers, and pit merger in stainless steel: 3D peridynamic models. Corros Sci 150:17–31
30. Jafarzadeh S, Chen Z, Bobaru F (2019) Computational modeling of pitting corrosion. Corros Rev 37(5): 419–439. https://doi.org/10.1515/corrrev-2019-0049
31. Silling SA (2014) Origin and effect of nonlocality in a composite. J Mech Mater Struct 9(2):245–258
32. Silling SA (2016) Why peridynamics? In: Bobaru F, Foster JT, Geubelle PH, Silling SA (eds) *Handbook of Peridynamic Modeling* (pp. 41-62). Chapman and Hall/CRC, Boca Raton
33. Silling SA, Askari E (2005) A meshfree method based on the peridynamic model of solid mechanics. Comput Struct 83(17–18):1526–1535
34. Seleson P, Littlewood DJ (2016) Convergence studies in meshfree peridynamic simulations. Comput Math Appl 71(11):2432–2448
35. Macek RW, Silling SA (2007) Peridynamics via finite element analysis. Finite Elem Anal Des 43(15):1169–1178

36. De Meo D, Oterkus E (2017) Finite element implementation of a peridynamic pitting corrosion damage model. Ocean Eng 135:76–83
37. Chen X, Gunzburger M (2011) Continuous and discontinuous finite element methods for a peridynamics model of mechanics. Comput Methods Appl Mech Eng 200(9–12):1237–1250
38. Du Q, Tian L, Zhao X (2013) A convergent adaptive finite element algorithm for nonlocal diffusion and peridynamic models. SIAM J Numer Anal 51(2):1211–1234
39. Ren B, Wu C, Askari E (2017) A 3D discontinuous Galerkin finite element method with the bond-based peridynamics model for dynamic brittle failure analysis. Inter J Impact Engin 99:14–25
40. Kilic B, Madenci E (2010) Coupling of peridynamic theory and the finite element method. J Mech Mater Struct 5(5):707–733
41. Galvanetto U, Mudric T, Shojaei A, Zaccariotto M (2016) An effective way to couple FEM meshes and peridynamics grids for the solution of static equilibrium problems. Mech Res Commun 76:41–47
42. Canuto C, Hussaini MY, Quarteroni A, Thomas A Jr (2012) *Spectral methods in fluid dynamics*. Springer Science & Business Media, Berlin
43. Cooley JW, Tukey JW (1965) An algorithm for the machine calculation of complex Fourier series. Math Comput 19(90):297–301
44. Frigo M, Johnson SG (2005) The design and implementation of FFTW3. Proc IEEE 93(2):216–231
45. Du Q, Yang J (2016) Asymptotically compatible Fourier spectral approximations of nonlocal Allen–Cahn equations. SIAM J Numer Anal 54(3):1899–1919
46. Sharma L, Peerlings RH, Shanthraj P, Roters F, Geers MG (2018) FFT-based interface decohesion modelling by a nonlocal interphase. Adv Model Simul Engin Sci 5(1):7
47. Du Q, Yang J (2017) Fast and accurate implementation of Fourier spectral approximations of nonlocal diffusion operators and its applications. J Comput Phys 332:118–134
48. Coclite GM, Fanizzi A, Lopez L, Maddalena F, Pellegrino SF (2018) Numerical methods for the nonlocal wave equation of the peridynamics. Appl Numer Math. https://doi.org/10.1016/j.apnum.2018.11.007
49. Slevinsky RM, Montanelli H, Du Q (2018) A spectral method for nonlocal diffusion operators on the sphere. J Comput Phys 372:893–911
50. Alali, B., & Albin, N. (2019). Fourier spectral methods for nonlocal models. *arXiv preprint arXiv: 1907.11998*
51. Bueno-Orovio A, Kay D, Burrage K (2014) Fourier spectral methods for fractional-in-space reaction-diffusion equations. BIT Numer Math 54(4):937–954
52. Wang H, Tian H (2014) A fast and faithful collocation method with efficient matrix assembly for a two-dimensional nonlocal diffusion model. Comput Methods Appl Mech Eng 273:19–36
53. Wang H (2018) Peridynamics and nonlocal diffusion models: fast numerical methods. In: Voyiadjis GZ (ed) *Handbook of Nonlocal Continuum Mechanics for Materials and Structures* (Vol. 2). Springer International Publishing, Berlin, pp 1331–1352. https://doi.org/10.1007/978-3-319-22977-5_35-1
54. Kevlahan NK-R, Ghidaglia J-M (2001) Computation of turbulent flow past an array of cylinders using a spectral method with Brinkman penalization. Euro J Mech-B/Fluids 20(3):333–350
55. Bueno-Orovio A, Perez-Garcia VM, Fenton FH (2006) Spectral methods for partial differential equations in irregular domains: the spectral smoothed boundary method. SIAM J Sci Comput 28(3):886–900
56. Yu HC, Chen HY, Thornton K (2012) Extended smoothed boundary method for solving partial differential equations with general boundary conditions on complex boundaries. Model Simul Mater Sci Eng 20(7): 075008
57. Brinkman H (1949) A calculation of the viscous force exerted by a flowing fluid on a dense swarm of particles. *Flow, Turbulence and Combustion* 1(1):27
58. Angot P, Bruneau C-H, Fabrie P (1999) A penalization method to take into account obstacles in incompressible viscous flows. Numer Math 81(4):497–520
59. Schneider K (2005) Numerical simulation of the transient flow behaviour in chemical reactors using a penalisation method. Comput Fluids 34(10):1223–1238
60. Kolomenskiy D, Schneider K (2009) A Fourier spectral method for the Navier–Stokes equations with volume penalization for moving solid obstacles. J Comput Phys 228(16):5687–5709
61. Schneider K, Neffaa S, Bos WJ (2011) A pseudo-spectral method with volume penalisation for magneto-hydrodynamic turbulence in confined domains. Comput Phys Commun 182(1):2–7
62. Kadoch B, Kolomenskiy D, Angot P, Schneider K (2012) A volume penalization method for incompressible flows and scalar advection–diffusion with moving obstacles. J Comput Phys 231(12):4365–4383
63. Engels T, Kolomenskiy D, Schneider K, Lehmann F-O, Sesterhenn J (2016) Bumblebee flight in heavy turbulence. Phys Rev Lett 116(2):028103
64. Ravi S, Kolomenskiy D, Engels T, Schneider K, Wang C, Sesterhenn J et al (2016) Bumblebees minimize control challenges by combining active and passive modes in unsteady winds. Sci Rep 6:35043

65. Du Q, Gunzburger M, Lehoucq RB, Zhou K (2012) Analysis and approximation of nonlocal diffusion problems with volume constraints. SIAM Rev 54(4):667–696
66. Radu P, Wells K (2019) A doubly nonlocal Laplace operator and its connection to the classical laplacian. J Integ Eq Appli 31(3):379–409. https://projecteuclid.org/euclid.jiea/1536804038
67. Zhao J, Chen Z, Mehrmashhadi J, Bobaru F (2018) Construction of a peridynamic model for transient advection-diffusion problems. Int J Heat Mass Transf 126:1253–1266
68. Du Q, Gunzburger M, Lehoucq RB, Zhou K (2013) A nonlocal vector calculus, nonlocal volume-constrained problems, and nonlocal balance laws. Mathematical Models and Methods in Applied Sciences 23(03):493–540
69. Oterkus S, Madenci E, Agwai A (2014) Peridynamic thermal diffusion. J Comput Phys 265:71–96
70. Le Q, Bobaru F (2018) Surface corrections for peridynamic models in elasticity and fracture. Comput Mech 61(4):499–518
71. Aksoylu B, Celiker F, Kilicer O (2019) Nonlocal operators with local boundary conditions in higher dimensions. Adv Comput Math 45(1):453–492
72. Aksoylu B, Celiker F, Kilicer O (2018) Nonlocal operators with local boundary conditions: an overview. In: Voyiadjis GZ (ed) Handbook of Nonlocal Continuum Mechanics for Materials and Structures, vol 2, pp 1293–1330. https://doi.org/10.1007/978-3-319-22977-5_34-1
73. Rabiner, L. R., & Gold, B. (1975). Theory and application of digital signal processing. Englewood Cliffs, NJ, Prentice-Hall, Inc, 1975. 777 p
74. Proakis JG, Manolakis DG (1996) Digital signal processing: principles, algorithms, and applications (3rd Edition), 3rd edn. Prentice-hall international, inc, New Jersey
75. Canuto C, Hussaini MY, Quarteroni A, Zang TA (2006) Spectral methods. Springer, Berlin
76. Chen Z, Bobaru F (2015) Selecting the kernel in a peridynamic formulation: a study for transient heat diffusion. Comput Phys Commun 197:51–60
77. Whittaker, E. T., & Watson, G. N. (1996). A course of modern analysis: Cambridge University Press